Available online at www.sciencedirect.com

ScienceDirect

Acta Materialia 84 (2015) 110–123

Acta MATERIALIA

www.elsevier.com/locate/actamat

Mechanisms of subgrain coarsening and its effect on the mechanical properties of carbon-supersaturated nanocrystalline hypereutectoid steel

Y.J. Li,[a,*] A. Kostka,[a] P. Choi,[a] S. Goto,[a,b] D. Ponge,[a] R. Kirchheim[c] and D. Raabe[a,*]

[a]*Max-Planck Institut für Eisenforschung, Max-Planck-Str. 1, D-40237 Düsseldorf, Germany*
[b]*Department of Materials Science and Engineering, Faculty of Engineering and Resource Science, Akita University, Tegata Gakuencho, Akita 010-8502, Japan*
[c]*Institut für Materialphysik, Georg-August-Universität Göttingen, Friedrich-Hund-Platz 1, D-37077 Göttingen, Germany*

Received 3 August 2014; revised 10 October 2014; accepted 12 October 2014

Abstract—Carbon-supersaturated nanocrystalline hypereutectoid steels with a tensile strength of 6.35 GPa were produced from severely cold-drawn pearlite. The nanocrystalline material undergoes softening upon annealing at temperatures between 200 and 450 °C. The ductility in terms of elongation to failure exhibits a non-monotonic dependence on temperature. Here, the microstructural mechanisms responsible for changes in the mechanical properties were studied using transmission electron microscopy (TEM), TEM-based automated scanning nanobeam diffraction and atom probe tomography (APT). TEM and APT investigations of the nanocrystalline hypereutectoid steel show subgrain coarsening upon annealing, which leads to strength reduction following a Hall–Petch law. APT analyzes of the Mn distribution near subgrain boundaries and in the cementite give strong evidence of capillary-driven subgrain coarsening occurring through subgrain boundary migration. The pronounced deterioration of ductility after annealing at temperatures above 350 °C is attributed to the formation of cementite at subgrain boundaries. The overall segregation of carbon atoms at ferrite subgrain boundaries gives the nanocrystalline material excellent thermal stability upon annealing.
© 2014 Acta Materialia Inc. Published by Elsevier Ltd. All rights reserved.

Keywords: Cold-drawn pearlitic steel; Nanocrystalline steels; Strength softening; Annealing; Subgrain coarsening

1. Introduction

Cold-drawn pearlitic steel wires are important engineering materials for a variety of applications such as automobile tire cords, suspension bridge and power cables, piano strings, and springs due to their ultrahigh strength. In 1995 it was reported that severe cold-drawing of pearlite yields a tensile strength of 5 GPa [1]. In the following years the tensile strength of cold-drawn pearlitic steel wires has been increased to 6.35 GPa [2] and very recently even up to 7 GPa [3]. The extraordinary strength has made the materials attractive not only for engineering applications but also for studying basic relationships between structure and mechanical properties of nanoscaled alloys. During the past 50 years great efforts have been made to understand the microstructural evolution and its effect on strength upon cold drawing [3–9]. The most frequently reported finding is deformation-induced cementite decomposition [10–19] and its "unexpected" consequence on strain hardening, i.e. the decomposition of the hard phase—cementite—surprisingly does not adversely affect the material's strength. On the contrary, the tensile strength continuously increases upon cold drawing [3,4,20], even when the cementite has been significantly dissolved [3,18,19]. It is worth noting that the mechanism of deformation-induced cementite decomposition is still under dispute. Different from the assumption that the decomposition takes place upon cold drawing, due to the interaction between dislocations and carbon [3,18,19], Takahashi et al. [21] suggested that it mainly occurs upon low-temperature aging after cold drawing. With the development of characterization techniques such as Mössbauer spectroscopy [10], field ion microscopy (FIM) [11,15,22–25] and atom probe tomography (APT) [12–16,18,19] a deeper understanding of the mechanisms of cementite decomposition and their effects on microstructure and strength has been achieved. Among these characterization techniques APT is able to provide nano- and atomic-scale information on the carbon distribution in both cementite and ferrite with high compositional accuracy and statistical significance [2,19]. Recently, Li et al. [3] observed that above a true drawing strain of 4.19 the original lamellar ferrite/cementite structure in a hypereutectoid steel wire is gradually replaced by a 2-D nanoscaled ferrite subgrain structure upon further drawing. The dissolved carbon atoms were found to be

* Corresponding authors. Tel.: +49 211 6792853; fax: +49 211 6792333; e-mail addresses: y.li@mpie.de; d.raabe@mpie.de

http://dx.doi.org/10.1016/j.actamat.2014.10.027
1359-6462/© 2014 Acta Materialia Inc. Published by Elsevier Ltd. All rights reserved.

segregated at ferrite subgrain boundaries (SGBs), suppressing dynamic recovery and thus stabilizing the dislocation structure. Hence, the heavily deformed wires are no longer hypereutectoid pearlitic steels but carbon-supersaturated nanocrystalline hypereutectoid steels. At a true drawing strain of 6.52 the subgrain size has been reduced to below 10 nm, which provides a tensile strength of up to 7 GPa [3].

In many engineering applications such as suspension bridges and power cables cold-drawn hypereutectoid steel wires are subjected to hot-dip galvanization or blueing (a heat treatment to simulate the hot-dip galvanized process, up to 550 °C for 15 min after cold drawing) to improve their anti-corrosion property [26,27]. Such processes may reduce the tensile strength because the temperature during galvanizing can approach 500 °C [26,27]. Thus, it is essential to study the thermal stability of heavily cold-drawn pearlite as well as the microstructural mechanisms associated with strength reduction during annealing. The strength reduction of cold-drawn pearlite during annealing has been reported in Refs. [21,26–28,30]. Some results obtained by microstructural investigations using TEM and APT can be found in Refs. [13,26,28–30]. It is known that for the same heat-treatment condition the annealed microstructure of a material strongly depends on its microstructure prior to annealing. For cold-drawn pearlitic steels this prior microstructure, depending on the drawing strain ϵ_d, can be either a heterophase-dominated lamellar structure at low strains or a nanosized carbon-supersaturated ferrite subgrain-dominated dislocation structure at extremely high strains [3]. The materials investigated in the above-mentioned studies were mainly subjected to relatively low drawing strain, where the lamellar structure still prevails. The observations were often performed under relatively short and not sufficiently systematic annealing conditions. In this sense, the strength–microstructure relationships during annealing of cold-drawn pearlite have not yet been systematically studied, especially for wires with extremely high drawing strains.

Here we study the microstructure–property relationships of annealed carbon-supersaturated nanocrystalline hypereutectoid (0.98 wt.% C) steels produced from severely cold-drawn pearlite by a true strain ϵ_d of 6.0. This initial microstructure prior to annealing is significantly different from the materials studied in previous papers in which heterophase boundaries are still dominant [13,21,26–30]. The present work focuses mainly on the evolution of the nanoscaled subgrain structure in ferrite during annealing. More specifically, first, systematic investigations have been performed on the evolution of the nanosized ferrite subgrain structure during annealing. Second, quantitative analyzes of the subgrain structures in terms of area fractions of low-angle and high-angle grain boundaries have been performed as a function of the annealing temperature T_a using scanning nanobeam diffraction and the software ASTAR [31]. Third, subgrain coarsening is for the first time experimentally studied at the atomic scale and understood through triple-junction-controlled migration of subgrain boundaries. Finally, the effect of T_a on the ductility of annealed wires is also studied. The relationship between tensile strength and ferrite subgrain size can be described by a Hall–Petch law. On the basis of these investigations the effects of microstructural evolution on the mechanical properties of the carbon-supersaturated nanocrystalline steel upon annealing are discussed.

2. Experimental

2.1. Material and processing

The original pearlitic steel wires subjected to heavy cold drawing were of hypereutectoid composition (Fe–0.98C–0.31Mn–0.20Si–0.20Cr–0.01Cu–0.006P–0.007S in wt.% or Fe–4.40C–0.30Mn–0.39Si–0.21Cr–0.003Cu–0.01P–0.01S in at.%), and were provided by Suzuki Metal Industry Co. Ltd. Before cold drawing the wires were austenitized at 950 °C for 80 s followed by pearlitic transformation in a lead bath at 580 °C for 20 s and subsequent quenching in water. After this treatment specimens were subjected to cold drawing up to a true drawing strain of $\epsilon_d = 6.0$. The cold-drawn wire is characterized by a nanoscale ferrite subgrain structure associated with strong yet incomplete chemical decomposition of the cementite. The nanosized subgrains exhibit a two-dimensional columnar morphology which is elongated along the drawing direction. The subgrain size in the transverse cross-section (perpendicular to the wire axis) of the wire is 10 nm [3]. The carbon-supersaturated nanocrystalline steel samples were annealed for 30 min between 150 and 450 °C in 50 °C intervals. Short time annealing for 2 min was also performed at several selected temperatures.

2.2. Mechanical testing

The tensile strength of the annealed samples was measured at room temperature with a Dia Stron LEX 810 device at an initial strain rate of $\dot{\epsilon}_0 = 1.16 \times 10^{-3}\ s^{-1}$. The true tensile strain is determined by $\epsilon = \ln\frac{l_0+\Delta l}{l_0}$, where l_0 and Δl are the initial gauge length and the length change of the wires, respectively. The wire tensile elongation was measured by subtracting the machine elongation from the total length change. The true tensile stress is determined by $\sigma = \frac{F}{S_0}\cdot\exp(\epsilon)$, where F is the force and S_0 the initial cross-section of the wires.

2.3. Characterization techniques

A JEOL JEM-2200FS operated at 200 kV was applied to investigate the as-annealed samples in both TEM and scanning TEM (STEM) modes. Crystallographic orientation and phase mapping were performed by nanobeam diffraction in scanning mode using a transmission electron microscope equipped with a NanoMEGAS ASTAR system [31]. The scanning was conducted at 0.5 nm spot and 1.25 nm step size.

APT investigations were performed using a local electrode atom probe (LEAP 3000X HR™, Cameca Instruments) in voltage mode at 70 K, a pulse fraction of 15%, a pulse repetition rate of 200 kHz, and a detection rate of 0.005 atoms per pulse. Readers are referred to our previous works [2,19] regarding the detailed analyzes of APT data including chemical identification and 3-D reconstruction.

Samples for both TEM and APT were prepared using a dual-beam focused-ion-beam (FIB) (FEI Helios NanoLab 600TM). TEM investigations were performed on the cross-sections of wires. APT samples were prepared with their tips perpendicular to the wire axis according to the procedure described in Ref. [32] in order to reduce the local magnification effect [17,33] and to probe as many ferrite subgrains as possible.

A subgrain is here defined in this context as a grain without differentiating between low-angle (LAGBs) and high-angle grain boundaries (HAGBs). Its size d_{Sub} was measured through the line intercept method based on the APT and ASTAR data.

3. Results

3.1. Changes of strength and ductility upon annealing

Fig. 1(a) displays true tensile stress–strain curves of annealed cold-drawn wires at various T_a for 30 min. For each annealing condition three specimens were measured up to the point of fracture. The obtained average ultimate tensile strengths σ_{UTS} are presented as a function of T_a in Fig. 1(b), where data with lower drawing strains taken from the literature [21,26–28,30] are also plotted for comparison. It can be seen that the tensile strength at room temperature increases with ϵ_d so that the strength of the current material lies well above the literature data. With increasing annealing temperature all curves share a common feature, namely the strength starts to decrease beyond a critical temperature. Similar to pure metals the critical annealing temperature increases with decreasing ϵ_d. For highly prestrained wires with $\epsilon_d = 6.0$ the strength reduction occurs at $T_a > 150$ °C with a steep negative slope. In contrast, for slightly prestrained wires with $\epsilon_d = 1.7$ [26] and 1.9 [27] there is nearly no strength reduction up to 400 °C.

Fig. 1(c) shows that the annealing temperature has a non-monotonic influence on the ductility of the current material. At $T_a < 350$ °C the ductility increases with the annealing temperature, which is similar to pure metals upon annealing, where the materials regain work-hardening capability due to the recovery of deformation-induced defects such as dislocations and subgrain boundaries. The deterioration of ductility above 350 °C may be related to the reprecipitation and growth of cementite particles at subgrain boundaries during annealing. This issue will be further discussed in Section 4.4 based on APT observations.

3.2. TEM investigations of the evolution of nanosized ferrite subgrain structure with annealing temperature

Fig. 2 shows the STEM images in the transverse cross-section of annealed nanocrystalline hypereutectoid steel wires observed at various T_a for 2 and 30 min. After low-temperature annealing at 150 °C for 30 min the microstructure does not differ much from the as-cold-drawn state. The typical curled grain morphology in connection with the formation of a [0 1 1] fiber texture [34] evolved during cold drawing [2,13,15,35] still prevails (Fig. 2(a)). The remaining strong strain contrast hinders the identification of the nanosized ferrite subgrain structure by STEM. When annealed at 250 °C for 30 min (Fig. 2(b)) the ribbon-shaped structure becomes clearer. Neighboring lamellae consisting of ferrite subgrains with blurred boundaries can be distinguished from each other. In addition, a slight increase in the interlamellar spacing, which equals the transverse cross-sectional subgrain size [3], can be observed. At 350 °C for 2 min (Fig. 2(c)) the ribbon-shaped structure becomes less pronounced. Several isolated subgrains with clear boundaries can be recognized. When extending the annealing time to 30 min the whole subgrain structure becomes more distinctly visible (Fig. 2(d)). Each individual ferrite subgrain can be clearly distinguished (Fig. 2(d)). In addition, slight subgrain coarsening takes place. Upon annealing at 400 °C (Fig. 2(e)) and 450 °C (Fig. 2(f)) for 30 min significant subgrain coarsening occurs; however, the subgrain size is still below 100 nm.

Fig. 3 shows the ferrite subgrain structures observed by TEM at higher magnifications on as-annealed samples for $T_a \geq 350$ °C. Subgrains have coarsened significantly as compared to the as-drawn state. Zooming in on the regions highlighted with white squares reveals individual dislocations between neighboring subgrains (marked by red arrows), which prevail even at the highest annealing temperature of 450°. These observations suggest that a large volume fraction of LAGBs still exists after annealing.

Further quantitative measurements of the misorientation angle θ of subgrain boundaries and phase identification are performed by nanobeam diffraction in scanning mode using the ASTAR system [36]. Fig. 4 shows phase mappings of the wires annealed under various conditions. Green and black lines are LAGBS ($3° \leqslant \theta \leq 15°$) and HAGBs ($\theta > 15°$), respectively. The boundaries with $\theta \leq 3°$ are neglected due to orientation resolution. The results show that the two major microstructural features developed during severe cold drawing [2,3] prevail in the annealed samples. First, the columnar subgrain morphology still exists since no overlap of subgrain boundaries is observed in the transverse cross-section of the wires. Second, the initial lamellar structure has been replaced by nanoscaled ferrite subgrain structures with cementite particles located at subgrain boundaries and triple junctions. The presence of a large density of LAGBs in the ferrite is confirmed by the ASTAR orientation maps. Annealing at 250 °C for 30 min yields a fraction of LAGBs of 40% and a subgrain size of 16 ± 1.7 nm (Fig. 4(a)). At 450 °C the fraction of LAGBs decreases to 15% and the subgrain size coarsens to 53 ± 10 nm (Fig. 4(d)).

Cementite particles in the samples annealed at low temperatures were additionally investigated by means of high-resolution TEM (HRTEM). Fig. 5(a) and (b) show evidence of the presence of crystalline cementite after low-temperature annealing at 250 °C for 30 min and 350 °C for 2 min, respectively. The carbon content of the cementite particles has been further analyzed by APT measurements.

The fast Fourier transform analysis shown in Fig. 5(b) reveals stacking faults in the cementite. Since stacking faults are usually introduced by plastic deformation of cementite [37–39], the stacking faults observed here in the annealed sample are probably inherited from the cementite that remained after cold drawing. This result suggests that part of the remaining cementite may still maintain its crystalline structure after cold drawing.

3.3. APT investigations of the evolution of the nanosized ferrite subgrain structure as a function of the annealing temperature

Fig. 6 shows APT results in transverse cross-sectional views of the heavily cold drawn induced carbon-supersaturated nanocrystalline steel annealed at various conditions. Only carbon atoms (red dots) are displayed. Regions identified by green-colored isoconcentration surfaces are

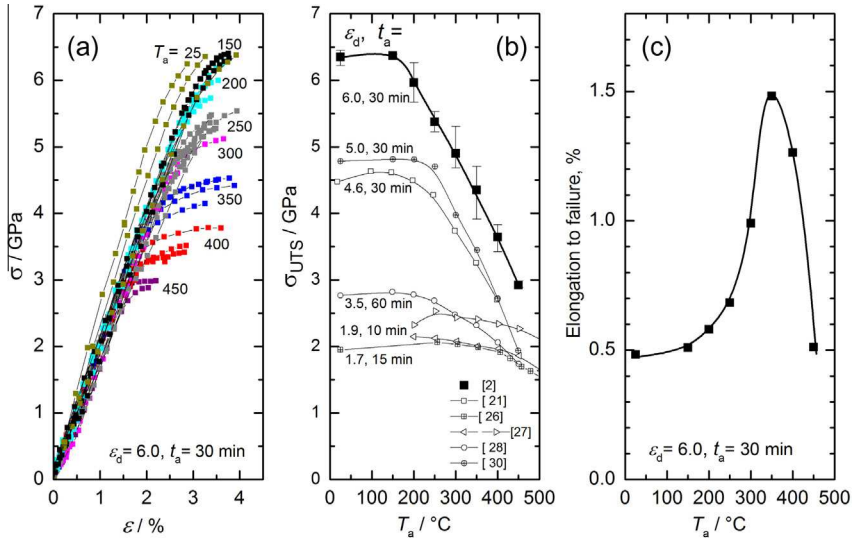

Fig. 1. (a) True tensile stress–strain curves of annealed nanocrystalline hypereutectoid steel wires at different annealing temperatures T_a for 30 min. (b) Maximum tensile stress vs. annealing temperature; data taken from the literature with different initial drawing strains and annealing times t_a [2,21,26–28,30] for comparison. (c) Influence of annealing temperature on the elongation to failure derived from (a).

cementite, as will be confirmed later. The nanoscaled subgrain structure with carbon segregating at subgrain boundaries was inherited from the as-cold-drawn state. The subgrain size d_{sub} increases with increasing T_a and t_a, which is consistent both with the STEM observations and the ASTAR measurements. The influence of the annealing temperatures on the carbon concentrations in ferrite and cementite is quantified by using proximity histograms across ferrite–cementite interfaces. The results in Fig. 7 show that carbon has reached the stoichiometric concentration of 25 at.% in the cementite formed in the as-annealed states already at 250 °C for 30 min. Correspondingly, the carbon concentration in ferrite decreases with the annealing temperature, indicating that more carbon atoms partition from ferrite into cementite with increasing T_a, and thus the volume fraction of cementite increases. The stoichiometric carbon concentration inside cementite together with its crystalline structure (revealed in Fig. 5) identify the regions enclosed by the isoconcentration surfaces in Fig. 6 as crystalline cementite.

In comparison to carbon the concentration of Mn in both ferrite and cementite is strongly temperature dependent. Up to annealing at 350 °C for 2 min a homogeneous distribution of Mn throughout both the ferrite and cementite phases, as a consequence of mechanical alloying during cold drawing [40], is detected. When extending t_a to 30 min, slight partitioning of Mn into cementite adjacent to ferrite–cementite interfaces can be observed (see blue curve in Fig. 7). Further enhancing T_a leads to stronger partitioning of Mn into the cementite. However, it is worth noting that even after annealing at the highest T_a of 450 °C studied here, the incoming flux of Mn from the ferrite cannot be accommodated throughout the cementite. We attribute this saturation behavior to a kinetic freezing effect (smaller diffusion coefficient in cementite than in ferrite) as reported in Refs. [2,40]. Regarding the detailed distributions of other alloying elements, such as Si and Cr, readers are referred to Refs. [21,40].

Fig. 8 shows the distribution of Mn (green dots) in the samples annealed at $T_a \geq 350$ °C. The distribution of Fe (blue dots) is also displayed as a reference. Fe is observed to be homogeneously distributed in ferrite for all annealing conditions. After annealing at 350 °C for 2 min, a similarly homogeneous distribution of Mn is observed throughout the whole detected volume, including ferrite and cementite, as also seen from the concentration profile in Fig. 7 (pink line). After annealing at 400 °C for 2 min some Mn-depleted zones appear near subgrain boundaries, as indicated by arrows in Fig. 8(b). After annealing for 30 min at the same temperature the Mn-depleted zones with a width of 10–20 nm become significant (see arrows in Fig. 8(c)). In addition, the Mn-depleted zones do not symmetrically appear on both sides but only on one side of the subgrain boundaries. It is worth noting that the observation of a continuous distribution of Fe (without any depletion near the subgrain boundaries) rules out the possibility of attributing the non-symmetrical Mn-depleted zones to lens artifacts associated with the APT measurements [41–45]. A possible explanation of this phenomenon will be discussed in Section 4.2.

Fig. 9 displays the ultimate strength of annealed samples, σ_{UTS}, as a function of the reciprocal of the square root of the subgrain size d_{Sub} of the as-annealed states (red symbols). This relationship is referred to as the Hall–Petch relation. In the context of heavily cold-drawn pearlite wires the Hall–Petch relationship has been commonly used to describe the strength increase in terms of the gradual reduction in the average lamellar spacing between the ferrite and the cementite [4]. The internal heterophase interfaces impede dislocation movement and multiplication and hence strengthen the material. The data for the same wires in the as-cold-drawn state [3] are also displayed for comparison (black symbols). Surprisingly, the σ_{UTS}–$d_{Sub}^{-0.5}$ relationship for as-annealed wires also obeys a Hall–Petch law with a slope k_{HP} of 621 MPa μm$^{0.5}$. Moreover, the k_{HP}-value for the annealed materials is slightly smaller than that for the as-cold-drawn materials, i.e. the annealed materials are stronger than the cold-drawn wires for the same subgrain size. The k_{HP} value, which is affected by the carbon concentration at the grain boundary, has been reported to be in

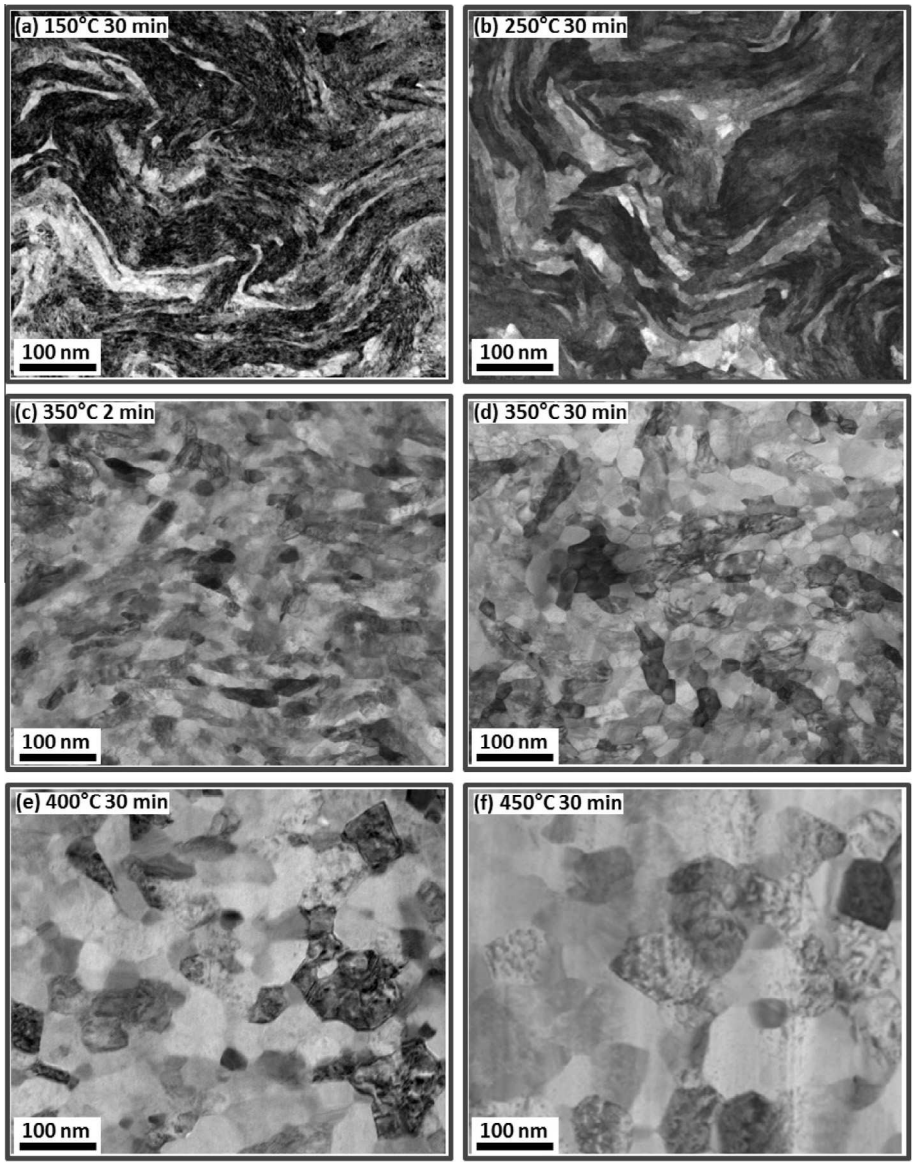

Fig. 2. STEM images of heat-treated nanocrystalline hypereutectoid steel wires in transverse cross-sections showing evolution and coarsening of the nanosized subgrain structures during annealing.

the range between 315 and 760 MPa $\mu m^{0.5}$ [46–50]. While the ferrite grain size investigated in the literature was in the micrometer range [46–50], it is interesting to observe that the current value observed in the nanocrystalline steel also falls in the reported range.

4. Discussion

As mentioned in Section 1, the microstructures prior to annealing are strongly dependent on the drawing strain ϵ_d. They differ from each other not only in the defect density and interlamellar spacing, but also in the morphology and the volume fractions of the phase constituents. For the wires with low and moderate drawing strains lamellar structures are still dominant despite the cementite decomposition [13,21,26–30]. For the present case with extremely high drawing strain of 6.0 a significant decomposition of cementite has occurred and the original lamellar structure has been replaced by a carbon-supersaturated ferrite subgrain structure [3]. Furthermore, once the ferrite subgrain structure becomes dominant it controls the strength of materials not only during further cold drawing [3] but also upon annealing. As shown in Section 3, ferrite subgrain coarsening is evidently a major reason for the strength reduction upon annealing. Thus, we will focus in the following on understanding the mechanisms of subgrain coarsening and its influence on the mechanical properties. The unexpected phenomenon of the observed ductility deterioration with increasing T_a is also briefly discussed.

4.1. Dislocation annihilation and rearrangement

Severely cold drawing the pearlitic steel wires yields a ribbon-shaped ferrite structure containing nanosized subgrains, whose boundaries along the longer edges of the ribbons have high misorientation angles, which can still be recognized after annealing at 250 °C for 30 min

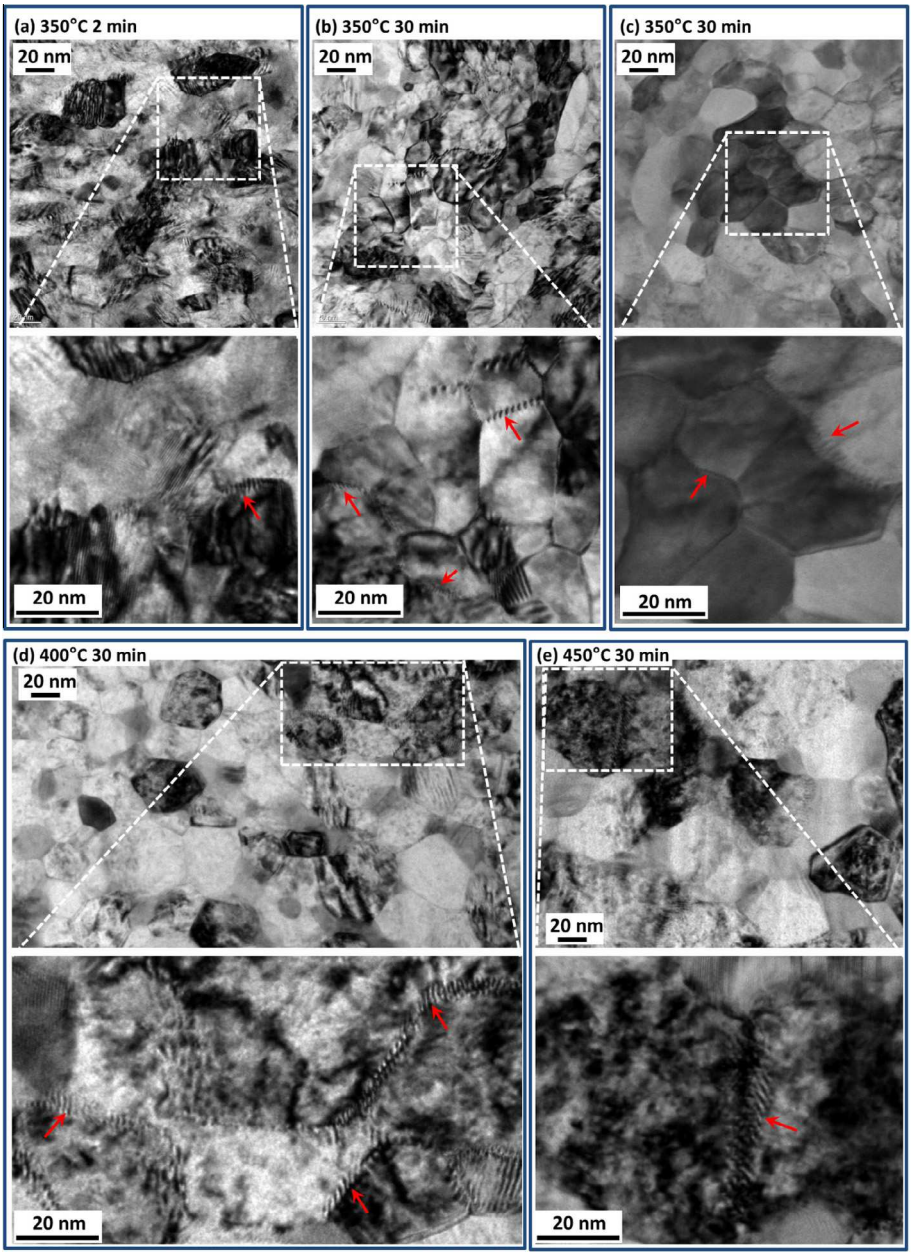

Fig. 3. TEM images of heat-treated nanocrystalline hypereutectoid steel wires in transverse cross-sections revealing the nanosized ferrite subgrain structures. Images at high magnification show dislocation arrays forming low-angle grain boundaries (marked by red arrows). (For interpretation of the references to color in this figure legend, the reader is referred to the web version of this article.)

(Fig. 4(a)). In connection with the formation of a strong [0 1 1] wire texture [3,34,51,52], the subgrain boundaries connecting the neighboring longer edges of the ribbons should be mainly of tilt type with low misorientation angles [53]. The STEM investigation indicates that 40% of subgrain boundaries are LAGBs after annealing at 250 °C for 30 min. If the magnitude of the misorientation angles between all boundaries are disregarded, the subgrains exhibit equiaxed morphology in the cross-section of the wire [3]. The HAGBs in severely deformed materials, due to their strong interactions with dislocations and the high internal stresses, are generally believed to be in a non-equilibrium state, yielding very high lattice distortions in their vicinity. When the grain size is reduced down to several tens of nanometers, the distortion zone can extend into the grain interiors [54]. This strong distortion makes an identification of the grain boundaries by TEM methods difficult.

After annealing at 150 °C for 30 min no reduction in strength is observed (Fig. 1(b)). After annealing at 250 °C for 30 min, the material strength is somewhat reduced, but still remains at a level around 5.5 GPa, indicating that no significant microstructural changes occurred. It is also noticed that the carbon concentration in ferrite after annealing at this temperature is distinctly higher than the values measured at higher temperatures (Fig. 7 top). This result is consistent with the observation of a small size and low volume fraction of cementite as shown in Figs. 4(a) and 6(a), meaning that a considerable formation, i.e. reprecipitation, of cementite at the expense of solute carbon atoms in the ferrite did not happen. The main

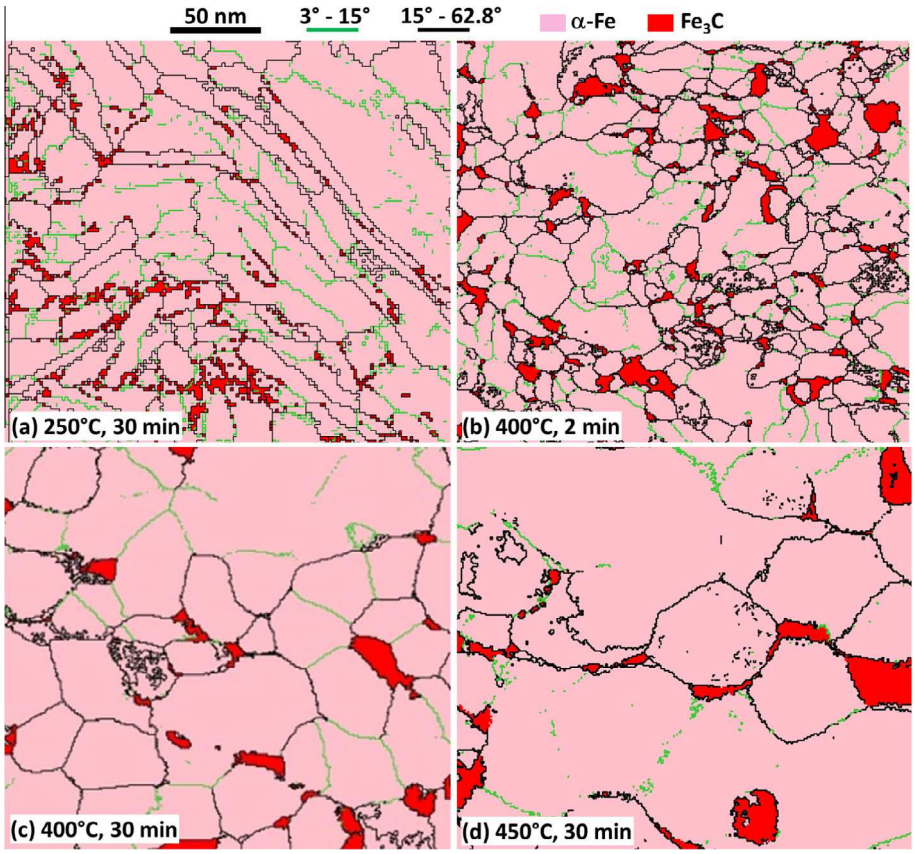

Fig. 4. Phase maps obtained via scanning nanobeam TEM diffraction (ASTAR) for heat-treated nanocrystalline hypereutectoid steel wires in the transverse cross-section. Green and black lines are for subgrain boundaries with misorientation angles of 3–15° and 15–62.8°, respectively. (For interpretation of the references to color in this figure legend, the reader is referred to the web version of this article.)

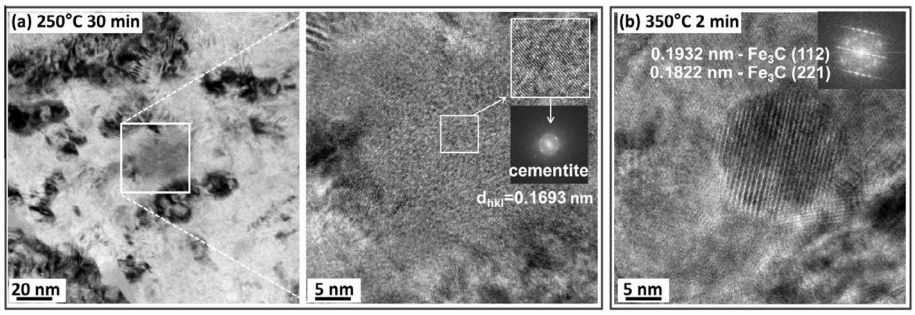

Fig. 5. TEM images showing crystalline cementite after annealing at (a) 250 °C for 30 min and (b) 350 °C for 2 min. Fast Fourier transform (FFT) analyzes reveal the presence of stacking faults inside of the cementite.

microstructural change upon annealing at a temperature below 250 °C for 30 min is thus attributed to partial annihilation of dislocations in the cell walls and near subgrain boundaries, where dislocations of opposite sign can recombine and disappear. The remaining dislocations of the same sign rearrange into low-energy configurations by forming new subgrain boundaries or by being integrated into existing LAGBs. This process results in a partial relaxation of the non-equilibrium structure of the existing HAGBs and a reduction of internal elastic stresses so that the visibility of the subgrain boundaries inside the curled lamellae is improved (Fig. 2(b)). On the other hand, the relaxation of non-equilibrium grain boundaries may induce a strengthening effect by limiting dislocation emission (see Section 4.3 for a further discussion), which compensates the softening effect due to dislocation annihilation so that the materials' strength does not significantly decrease. The slight increase in subgrain size is considered mainly due to the rearrangement of dislocations.

Above annealing temperatures of 350 °C subgrain coarsening becomes the major microstructural phenomenon. In the next section, the mechanism of subgrain coarsening will be further discussed.

4.2. Boundary migration induced subgrain coarsening

Subgrain coarsening may occur through coalescence of the neighboring subgrains [55] or migration of boundaries

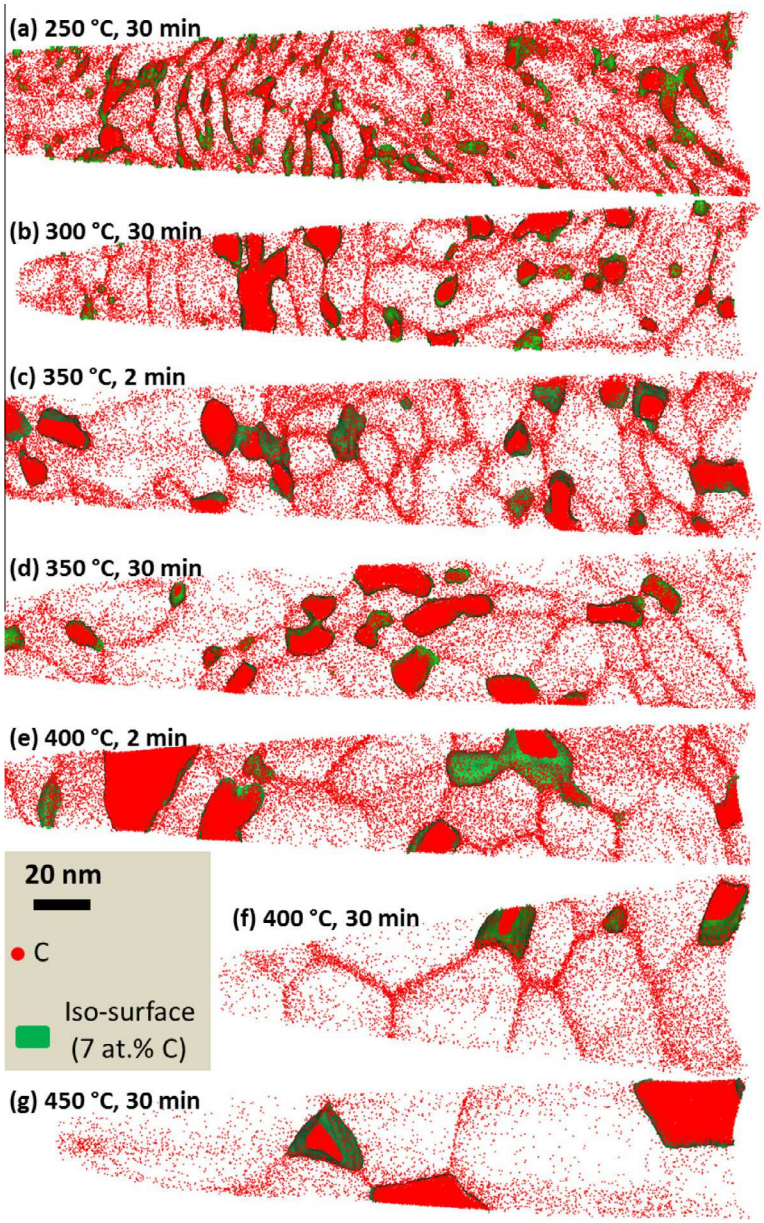

Fig. 6. 3-D carbon atom maps of heat-treated nanocrystalline hypereutectoid steel wires in transverse cross-section views. The isoconcentration surfaces for 7 at.% C are shown in green. (For interpretation of the references to color in this figure legend, the reader is referred to the web version of this article.)

[56–59]. The latter process is commonly assumed to be the major underlying mechanism of subgrain coarsening. Before discussing mechanisms of subgrain coarsening in the current microstructure, we recall the main features observed in association with the depletion of Mn near some of the subgrain boundaries (Fig. 8). First, the depletion area is asymmetrical around the subgrain boundaries; second, the degree of depletion is thermally activated, since it is stronger the higher the annealing temperature and the longer the annealing time. Annealing at 400 °C for 30 min yields Mn depletion zones of $\sim 10-20$ nm in width around the subgrain boundaries. This phenomenon can hardly be explained by segregation of Mn at subgrain boundaries through bulk diffusion. The Mn diffusion distance in the ferrite matrix can be estimated as $x = \sqrt{6Dt}$. Taking the bulk diffusivity $D_{\alpha}^{\mathrm{Mn}} = 2.4\times 10^{-23}$ m^2 s^{-1} [60] at 400 °C and an annealing time of 30 min results in a diffusion distance of about 0.5 nm, which is far below the observed value of $\sim 10-20$ nm. In addition, even if the long diffusion distance could be achieved by bulk diffusion, symmetrical Mn-depleted zones would have formed on both sides of the subgrain boundaries. Therefore, we propose that the observed asymmetric Mn-depleted zones are the result of migration of subgrain boundaries, which sweep and accumulate Mn atoms into the boundaries during migration. Due to the low diffusivity in ferrite the Mn atoms behind the swept zones cannot readily redistribute into the depleted zones to recover a local chemical equilibrium, i.e. the zones behind the moving subgrain boundaries remain depleted in Mn. This mechanism suggests a grain boundary migration related non-equilibrium segregation process that leads to an enrichment of Mn atoms at moving ferrite subgrain boundaries.

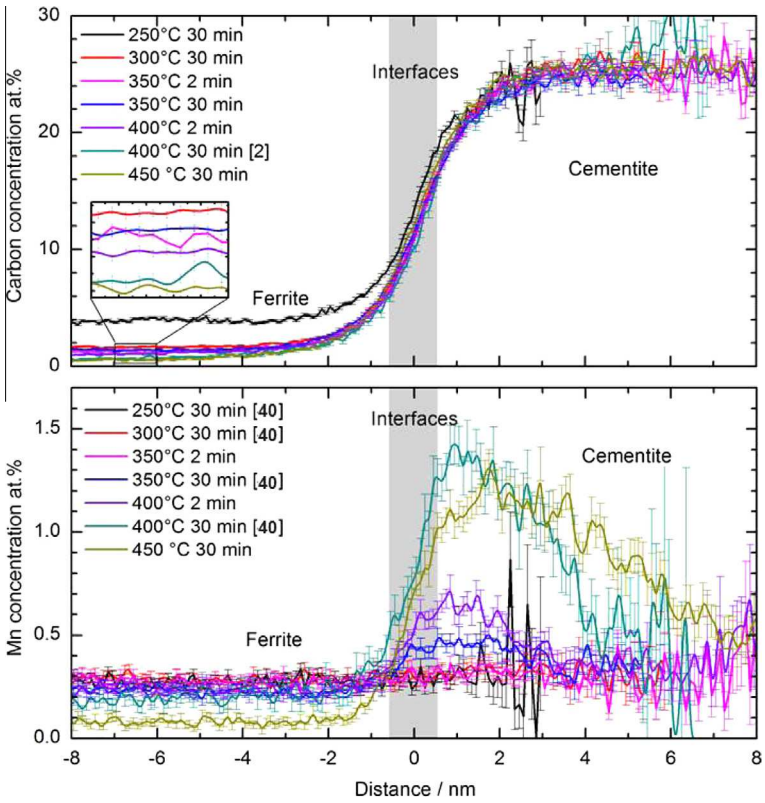

Fig. 7. Proximity histograms of C (top) and Mn (bottom) obtained from multiple interfaces (enclosed region > 6 nm) shown in Fig. 6 for as-annealed wires at various annealing temperatures and times. (Inset) An enlarged image showing the C concentrations in the ferrite. (For interpretation of the references to color in this figure legend, the reader is referred to the web version of this article.)

However, in the present case, strong segregation of Mn at subgrain boundaries was not observed. Instead, accompanying the depletion of Mn near the subgrain boundaries, the partitioning of Mn into the cementite becomes more pronounced and the Mn concentration in the ferrite decreases (Fig. 7 bottom). The apparent correlation between these observations would suggest that the Mn atoms are first accumulated at subgrain boundaries by boundary migration, and then diffuse along the subgrain boundaries into the cementite. It is known that Mn is a carbide-forming element and that its solubility in cementite is much higher than that in ferrite at 400 °C according to ThermalCalc calculations [2,40]. Clearly, the difference in solubility yields a thermodynamic driving force that promotes diffusion of Mn from ferrite into cementite. The only question is how the partitioning process kinetically works. Fig. 7 bottom shows that in the center of the cementite particles the Mn concentration approximately equals the value measured inside the ferrite. This is due to the fact that the Mn atoms originally remaining in the ferrite were automatically incorporated into the cementite particles upon growth when the cementite was formed in paraequilibrium. In the regions near the ferrite–cementite interface a much higher concentration of Mn was built up inside the cementite. After annealing at 400 °C for 30 min the Mn concentration in the cementite adjacent to the ferrite–cementite interfaces is about 7 times that in ferrite (Fig. 7 bottom). Recalling that the bulk diffusion distance at this annealing condition is only about 0.5 nm, the sluggish bulk diffusion cannot be the reason for the substantial partitioning of Mn into cementite. Instead, it can only be attributed to fast diffusion of Mn through subgrain boundaries and triple junctions. In summary, the most likely mechanism for the depletion of Mn near the subgrain boundaries and the partitioning of Mn into cementite is suggested to proceed in terms of two processes: first, Mn atoms are captured at subgrain boundaries by boundary migration; second, the captured Mn atoms diffuse along the subgrain boundaries or triple junctions into cementite. A similar sweeping mechanism has been proposed by Uray and Menyhárd to explain the segregation of iron at grain boundaries and second-phase particles in tungsten [61]. However, their analysis was performed on the basis of an indirect measurement of electrical resistivity. The current work gives direct evidence of the existence of this mechanism at the atomic scale.

The above discussion has demonstrated that Mn depletion near subgrain boundaries together with partitioning of Mn into cementite can serve as an indicator for boundary migration. Fig. 10 schematically shows two typical examples taken from Fig. 8(c). Fig. 10(a) shows three grains sharing a triple junction line (perpendicular to the page in 3-D). As a convention the grain boundaries between neighboring grains G_i and G_j are defined as G_i–G_j. The Mn-depleted zone exists in grain 1 and near the boundaries G1–G2 and G1–G3, but not near the GB G2–G3. This observation suggests that boundary G2–G3 did not move during annealing, and boundaries G1–G2 and G1–G3 together with their respective triple junctions moved along G2–G3. Consequently, the boundary G2–G3 becomes shorter while grain G1 coarsens and grains G2 and G3 shrink. Similarly, the movement of the two triple junctions

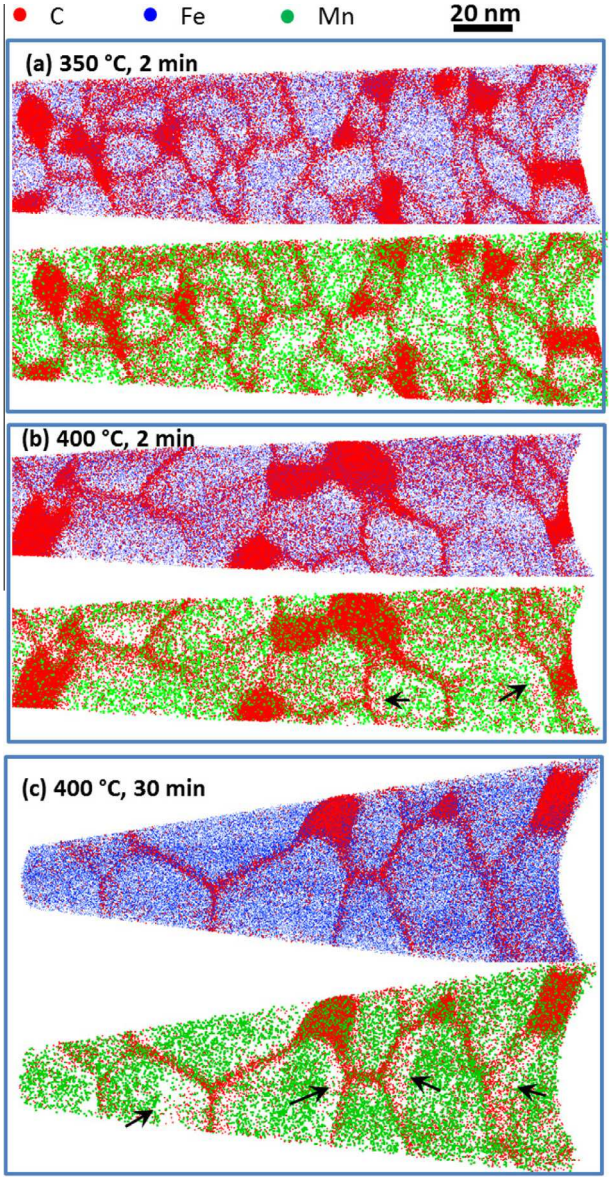

Fig. 8. Distributions of C (red), Fe (blue), and Mn (green) atoms in the nanosized ferrite subgrain structures with carbon segregation and spheroidized cementite at subgrain boundaries. Black arrows mark the possible original locations of subgrain boundaries which migrate during annealing. (For interpretation of the references to color in this figure legend, the reader is referred to the web version of this article.)

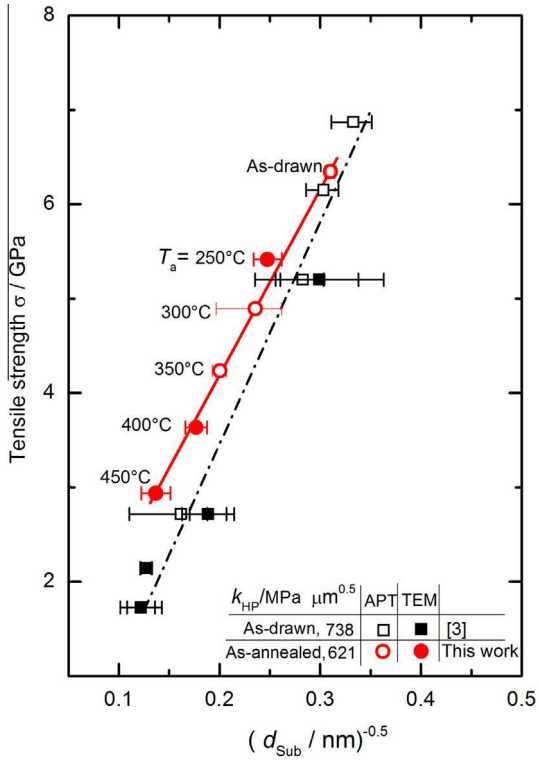

Fig. 9. Tensile strength vs. the reciprocal square root of the ferrite subgrain size d_{Sub} for heat-treated nanocrystalline hypereutectoid steel wires produced by cold drawing at $\epsilon_d = 6$ (red circles). Data for as-drawn wires [3] are shown for comparison. (For interpretation of the references to color in this figure legend, the reader is referred to the web version of this article.)

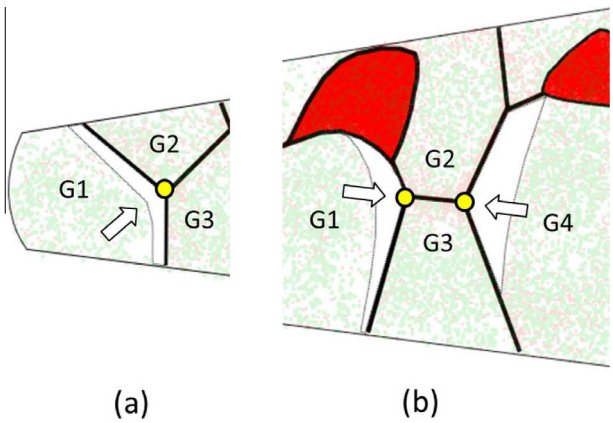

Fig. 10. (a and b) Subgrain structures schematically superimposed on selected areas taken from the left part and middle part of Fig. 8, respectively. White areas mark Mn-depleted regions and yellow full circles represent triple junctions among grains labeled with G1–G4. Arrows indicate the migration direction of the triple junctions. (For interpretation of the references to color in this figure legend, the reader is referred to the web version of this article.)

towards each other, shown in Fig. 10(b), leads to the coarsening of the grains G1 and G4, and the shrinkage of G2 and G3. Thus the Mn decoration and depletion patterns indicate the movement of the grain boundaries in the current microstructure.

The segregation of Mn in cementite as shown in Fig. 7 bottom, together with the atom map shown in Fig. 8, indicate that only slight boundary migration occurs upon annealing at 350 °C for 2 min. Above this condition the boundary migration becomes stronger with higher temperature. However, even at the highest investigated temperature of 450 °C the annealed subgrain size remains below 100 nm. This is believed to be mainly due to the effect of solute segregation at subgrain boundaries, which significantly reduces the grain boundary energy and thus the driving force for coarsening [62,63]. An additional limiting factor of grain coarsening in the current nanostructured material may be due to a drag effect associated with the triple junction lines. Traditionally, triple junctions are considered to have very high, even practically infinite, mobility so that they have little influence on boundary migration.

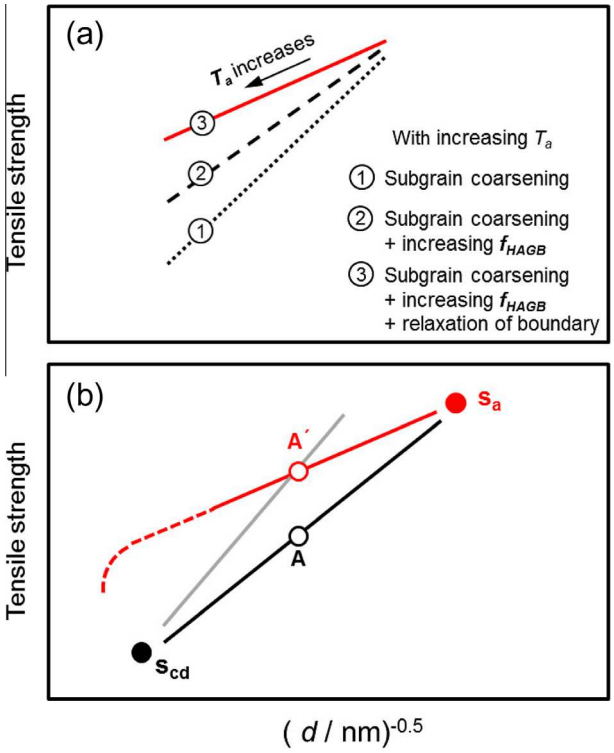

Fig. 11. Schematic diagrams showing the influence of (a) the annealing-induced changes in subgrain boundary character and (b) the starting point on the Hall–Petch slope. T_a is the annealing temperature. f_{HAGBs} is the volume fraction of HABGs. S_{cd} and S_a represent the starting points for cold drawing and annealing, respectively. A and A′ represent the data for cold-drawn and as-annealed materials, respectively, which have the same subgrain size.

Galina et al. [64] first proposed that triple junctions might have finite mobility. Recently, molecular dynamics simulations performed by Upmanyu et al. [65] suggested that the mobility of triple junctions in nanocrystalline materials can be sufficiently small to determine the rate of grain boundary migration. Gottstein et al. [66] theoretically studied the role of triple junctions on grain growth in nanocrystalline materials. They demonstrated on nanocrystalline Pd that triple junction drag could significantly slow down the growth of Pd grains. In the present case, a drag effect of triple junctions on grain growth may also exist due to the nanoscaled subgrain size. A third stabilizing effect on subgrain coarsening in the present case might be due to the formation of cementite particles at subgrain boundaries and at triple junctions, which renders further movement of boundaries difficult.

4.3. Modified Hall–Petch relationship applied to the annealed carbon-supersaturated nanocrystalline hypereutectoid steel

In our recent work [3] we reported that during cold drawing of pearlite the ferrite–cementite lamellar structure still prevails up to a strain range $\epsilon_d \leq 4.19$. Above this drawing strain the ferrite subgrain structure becomes dominant and dynamic recovery is strongly suppressed due to segregation of carbon at nanosized ferrite subgrain boundaries. As a result, the subgrain size continuously decreases upon further straining and the corresponding tensile strength increases following a Hall–Petch relation (see Fig. 9 and also Ref. [3]). After annealing it is interesting to observe that the annealed material with its reduced strength and coarser subgrain structure also follows a Hall–Petch law (Fig. 9), indicating that subgrain coarsening is the main reason for the strength reduction.

When comparing the strength–size relationships recorded for annealed and cold-drawn materials, it is noticed that the Hall–Petch slope k_{HP} for the annealed material is smaller than that of the deformed material and the annealed material is stronger than the deformed one for the same subgrain size. The explanation for this phenomenon lies in the fact that the annealed microstructure is not only substantially different from the lamellar structure that was still prevailing at low drawing strains, consisting of parallel and alternating ferrite and cementite layers, but also significantly deviating from the subgrain structure formed at high drawing strains. During annealing the cold-drawing induced ferrite subgrains further coarsen and spheroidal cementite particles form. Clearly, the heat-treatment process applied in the current study cannot bring the heavily deformed microstructure back to the initial structure through a reverse evolution by replacing the subgrain structure with a fine lamellar structure. Thus the variation of the tensile strength of specimens with annealed and hence coarsened subgrain structure is not necessarily expected to follow the same strength–size relationship as the wires with a lamellar structure. One of the reasons that renders the annealed samples mechanically stronger than the cold-drawn wires can be attributed to the increase in the subgrain boundary misorientation upon annealing, as shown in Fig. 4. Thus, in comparison to the deformed wires with the same subgrain size, the annealed structure contains a higher density of HAGBs, which are more efficient obstacles than LAGBs at hindering the penetration of dislocations through the grain boundaries.

Another probably even more important reason may be due to the relaxation of non-equilibrium grain boundaries upon annealing. It is known that the strength of nanocrystalline materials is mainly controlled by grain boundaries, whose strengthening effect is twofold. On one hand, they act as effective obstacles against dislocation motion, leading to a direct strengthening. On the other hand, they provide additional dislocation sources because those sources, which are usually operative in the grain interior of coarse-grained materials, do not exist inside nanosized grains. During annealing the relaxation of non-equilibrium grain boundaries may render dislocation sources less active or even remove them from the grain boundaries. Consequently, the applied external load has to be increased to enable the emission of dislocations from grain boundaries. Thus, for the same subgrain size, this additional strengthening effect makes the annealed subgrain structure stronger than the deformed subgrain structure where grain boundaries remain at a higher energy level and the emission of dislocations is easier. The effect of relaxation of non-equilibrium grain boundaries on the strength of materials upon annealing has been studied by molecular dynamics simulations [67]. The authors reported that the relaxed grain boundaries are less prone to emit dislocations which enhances the materials' strength. Similar results on an annealing-enhanced strengthening effect were reported by Valiev et al. [68] in nanostructured Ti produced by high-pressure torsion, by Wang et at. [69] in electrodeposited nanocrystalline Ni and by Huang et al. [70] in nanosized Al produced by accumulative roll bonding.

Fig. 11(a) schematically summarizes the above-discussed strengthening effects due to the change in the grain boundary character upon annealing. Curve ① shows a "gedanken" Hall–Petch relation of annealed materials that experience only subgrain coarsening without any change in grain boundary character. The superposition of the enhanced obstacle effect of the grain boundaries on dislocation motion by increasing the volume fraction of HAGBs f_{HAGBs} (curve ②) and the enhanced difficulty of dislocation emission from boundaries due to annealing induced-boundary relaxation (curve ③) not only improve the final strength of the annealed material, but also reduce the Hall–Petch slope. At first sight this explanation seems to be contradictory to the common understanding that a higher strength of grain boundaries usually yields a higher Hall–Petch slope. In fact, there is no such interpretation conflict, though it should be noted that the starting points of the two Hall–Petch curves are different, as depicted below in Fig. 11(b). The starting point (S_{cd} in Fig. 11(b)) of the curve for the cold-drawn material (the black line) corresponds to the original lamellar structure prior to cold drawing. For the annealed material the curve starts from the cold-drawn state (S_a, red line in Fig. 11(b)). If S_{cd} is taken as the starting point for the annealed material, the line going through S_{cd} and A' (gray line) exhibits a higher slope than the dark line, which is consistent with our explanation that the strength of the grain boundaries of as-annealed materials is higher than that in the cold-drawn materials for the same grain size at A. However, considering that the annealed microstructure (with progressively coarser grain structure) is completely different from that of the original lamellar structure, a Hall–Petch plot starting from S_{cd} is not a suitable presentation format for the annealed material, and thus is not shown in Fig. 9. In addition, with further increasing annealing temperature, the occurrence of strong recrystallization would lead to grain structures with completely different boundary properties compared to those of both the recovered and cold-drawn states. Furthermore, grain boundaries may become less important and the strength can be mainly controlled by the dislocation activity in the grain interiors. In this case, it is reasonable to infer that the Hall–Petch relation may break down (see the curved red dashed line) above a certain annealing temperature.

A third strengthening mechanism which appears after annealing may be due to the formation of spheroidal cementite particles. Both STEM and APT investigations indicate that the cementite particles are predominantly located at triple junctions and subgrain boundaries. A similar result was reported by Takahashi et al. [21] who suggested that the reprecipitated cementite are located along the prior ferrite–cementite interfaces. The strengthening effect of these particles may be mainly attributed to their effect on hindering grain boundary migration rather than their interaction with dislocations. However, this interaction may have a strong influence on the ductility of the annealed material, as will be discussed below.

4.4. Non-monotonic change of ductility upon annealing

As shown in Fig. 1(c) the ductility of the annealed materials investigated under the selected annealing conditions exhibits a non-monotonic dependence on temperature. The ductility reaches a maximum after annealing at 350 °C. Below 350 °C it increases with the annealing temperature, which is similar to the usual annealing effect observed on deformed coarse-grained materials, i.e. the material becomes softer and more ductile. The same reasons also apply for the present case at $T_a < 350$ °C. As discussed above, the major microstructural changes occurring under these annealing conditions are the reduction in dislocation density, slight subgrain coarsening and concomitant relief of internal stresses. These combined effects partially recover the work-hardening potential of the wires.

Above 350 °C the ductility deteriorates with increasing temperature. This result is somewhat surprising, because the main microstructural changes occurring in this temperature range, namely subgrain coarsening and spheroidization of cementite, would tend to enhance the ductility. Spheroidization processing of conventional materials (in contrast to nanosized materials) usually results in a homogeneous dispersion of cementite particles throughout the ferrite grains. This structure contains less total interface area per unit volume in spheroidized compared to lamellar pearlite and provides the material with a continuous ferrite matrix. Thus, plastic deformation of ferrite is less constrained by cementite and the material behaves more ductile. However, for the present carbon-supersaturated nanocrystalline steel the spheroidization of cementite, in particular at the high annealing temperatures, does not necessarily reduce the specific surface area of the cementite. In contrast, the reprecipitation and growth of new cementite particles leads to an increase in the area fraction of interfaces between ferrite and cementite. Furthermore, the increase of the subgrain size leads to a reduction of the volume fraction of the subgrain boundary area. This means that the ratio of the surface area of cementite to the area of subgrain boundary increases with increasing subgrain size. Hence, the structure consisting of larger subgrains contains a high fraction of the more brittle cementite particles at boundaries than that consisting of smaller grains. The influence of grain size on microcracking of grain boundary carbide was explained by Smith [71] in terms of a dislocation–carbide interaction model. The approach suggests that larger grains are more susceptible to microcracking of grain boundary carbides than smaller grains because more dislocations pile up inside the coarser grains, generating a higher stress concentration against the brittle grain boundary carbide.

5. Conclusions

After annealing at temperatures between 250 and 450 °C for 30 min, the carbon-supersaturated nanocrystalline hypereutectoid steel produced from severely cold-drawn pearlite exhibits significant temperature-dependent changes in microstructure, tensile strength and ductility. Based on TEM and APT investigations conducted on various annealed samples the mechanisms responsible for the microstructural evolution and its effect on the mechanical properties are discussed.

No strength reduction is observed for $T_a < 150$ °C. Strength softening due to dislocation annihilation and rearrangement may be compensated by relaxation of non-equilibrium grain boundaries which limits dislocation emission upon loading.

At annealing temperatures of $T_a > 250$ °C the tensile strength decreases and the subgrain size increases with T_a. The variation in tensile strength with subgrain size follows

a Hall–Petch relationship. Interestingly, the annealed wires are stronger than the cold-drawn samples for the same subgrain size. This result is correlated with the increasing area fraction of HAGBs and the relaxation of non-equilibrium grain boundaries, which makes penetration of dislocations through and emission of dislocations from grain boundaries more difficult, respectively.

The migration of triple junctions and subgrain boundaries is confirmed by APT mappings of the Mn distribution. It is evident that subgrain coarsening occurs through the migration of subgrain boundaries. Segregation of C atoms at the ferrite subgrain boundaries gives the nanoscaled subgrain structure excellent thermal stability.

The ductility increases first with increasing temperature up to 350 °C, then decreases with further increasing temperature. The deterioration of ductility is suggested to be associated with the formation and growth of cementite particles at ferrite subgrain boundaries.

Acknowledgments

The authors thank Dr. H. Yarita, Suzuki Metal Industry Co. Ltd., for providing the cold-drawn specimens. We are grateful to the Deutsche Forschungsgemeinschaft for co-sponsoring some of this research (SFB 602 and KI230/34–1).

References

[1] T. Takahashi, I. Ochiai, H. Tashiro, S. Ohashi, S. Nishida, T. Tarui, Nippon Steel Tech. Rep. 64 (1995) 45.
[2] Y.J. Li, P. Choi, S. Goto, C. Borchers, D. Raabe, R. Kirchheim, Acta Mater. 60 (2012) 4005.
[3] Y.J. Li, D. Raabe, M. Herbig, P. Choi, S. Goto, A. Kostka, et al., Phys. Rev. Lett. 113 (2014) 106104.
[4] J.D. Embury, R.M. Fisher, Acta Metall. 14 (1966) 147.
[5] D.A. Porter, K.E. Easterling, G.D.W. Smith, Acta Metall. 14 (1966) 147.
[6] M. Dollar, I.M. Bernstein, A.W. Thompson, Acta Metall. 36 (1988) 311.
[7] J.G. Sevillano, J. Phys. III 1 (1991) 967.
[8] D. Raabe, P. Choi, Y.J. Li, A. Kostka, X. Sauvage, F. Lecouturier, et al., MRS Bull. 35 (2010) 982.
[9] X.D. Zhang, A. Godfrey, X. Huang, N. Hansen, Q. Liu, Acta Mater. 59 (2011) 3422.
[10] V.N. Gridnev, V.G. Gavrilyuk, I.Y. Dekhtyar, Y.Y. Meshkov, P.S. Nizin, V.G. Prokopenko, Phys. Status Solidi A 14 (1972) 689.
[11] H.G. Read, W.T. Reynolds Jr., K. Hono, T. Tarui, Scripta Mater. 37 (1997) 1221.
[12] F. Danoix, D. Julien, X. Sauvage, J. Copreaux, Mater. Sci. Eng. A 250 (1998) 8.
[13] M.H. Hong, W.T. Reynolds Jr., T. Tarui, K. Hono, Metall. Mater. Trans. A 30 (1999) 717.
[14] X. Sauvage, J. Copreaux, F. Danoix, D. Blavette, Philos. Mag. A 80 (2000) 781.
[15] K. Hono, M. Ohnuma, M. Murayama, S. Nishida, A. Yoshie, Scripta Mater. 44 (2001) 977.
[16] C. Borchers, T. Al-Kassab, S. Goto, R. Kirchheim, Mater. Sci. Eng. A 502 (2009) 131.
[17] S. Sauvage, W. Lefebvre, C. Genevois, S. Ohsaki, K. Hono, Scripta Mater. 60 (2009) 1056.
[18] Y.J. Li, P. Choi, C. Borchers, Y.Z. Chen, S. Goto, D. Raabe, et al., Ultramicroscopy 111 (2011) 628.
[19] Y.J. Li, P. Choi, C. Borchers, S. Westerkamp, S. Goto, D. Raabe, R. Kirchheim, Acta Mater. 59 (2011) 3965.
[20] Y.Z. Chen, G. Csiszár, J. Cizek, S. Westerkamp, C. Borchers, T. Ungár, et al., Metall. Mater. Trans. A 44 (2013) 3882.
[21] J. Takahashi, M. Kosaka, K. Kawakami, T. Tarui, Acta Mater. 60 (2012) 387.
[22] T. Tarui, T. Takahashi, S. Ohashi, R. Uemori, Iron Steelmaker 21 (1994) 25.
[23] T. Tarui, J. Takahashi, H. Tashiro, S. Nishida, in: H.G. Paris, D.K. Kim (Eds.), Processing and Applications of Metal Wires, TMS, Warrendale, PA, 1996, p. 87.
[24] N. Maruyama, T. Tarui, H. Tashiro, Scripta Mater. 46 (2002) 599.
[25] T. Tarui, N. Maruyama, J. Takahashi, S. Nishida, H. Tashiro, Nippon Steel Technical Report No. 91, January 2005.
[26] K. Makii, H. Yaguchi, M. Kaiso, N. Ibaraki, Y. Miyamoto, Y. Oki, Scripta Mater. 37 (1997) 1753–1759.
[27] T. Tarui, S. Nishida, S. Yoshie, H. Ohba, Y. Asano, I. Ochiai, T. Takahashi, Nippon Steel Technical Report, vol. 80, 1999, pp. 44–49.
[28] J. Languillaume, G. Kapelski, B. Baudelet, Mater. Lett. 33 (1997) 241.
[29] J. Languillaume, G. Kapelski, B. Baudelet, Acta Mater. 45 (1997) 1201.
[30] C. Borchers, Y. Chen, M. Deutges, S. Goto, R. Kirchheim, Philos. Mag. Lett. 90 (2010) 581.
[31] P. Moeck, S. Rouvimov, E.F. Rauch, M. Véron, H. Kirmse, I. Häusler, et al., Acta Mater. 46 (2011) 589.
[32] J. Takahashi, T. Tarui, K. Kawakami, Ultramicroscopy 109 (2009) 193.
[33] X. Sauvage, L. Thilly, D. Blavette, J. Phys. IV France 11 (2001) 27.
[34] W.F. Hosford Jr., Trans. AIME 230 (1964) 12.
[35] G. Langford, Metall. Trans. 1 (1970) 465.
[36] M. Herbig, D. Raabe, Y.J. Li, P. Chio, S. Zeafferer, S. Goto, Phys. Rev. Lett. 112 (2014) 126103.
[37] W.F. Kindle, H.F. Trout, Metallography 3 (1970) 421.
[38] A. Inoue, T. Ogura, T. Masumoto, Mater. Trans. JIM 17 (1976) 149.
[39] L.E. Karkina, T.A. Zubkova, I.L. Yakovleva, Phys. Metals Metall. 114 (2013) 234.
[40] Y.J. Li, P. Choi, S. Goto, C. Borchers, D. Raabe, R. Kirchheim, Ultramicroscopy 132 (2013) 233.
[41] M.K. Miller, A. Cerezo, M.G. Hetherington, G.D.W. Smith, Atom Probe Field Ion Microscopy, Clarendon Press, Oxford, 1996.
[42] M.K. Miller, Atom Probe Tomography Analysis at the Atomic Scale, Kluwer Academic/Plenum, New York, 2000.
[43] T.F. Kelly, M.K. Miller, Rev. Sci. Instrum. 78 (2007) 031101.
[44] D. Seidman, Annu. Rev. Mater. Sci. 37 (2007) 127.
[45] E.A. Marquis, M.K. Miller, D. Blavette, S.P. Ringer, C.K. Sudbrack, G.D.W. Smith, MRS Bull. 34 (2009) 725.
[46] D.V. Wilson, Met. Sci. J. 1 (1967) 40.
[47] B. Mintz, Met. Technol. 11 (1984) 265.
[48] B. Mintz, H. He, G.D.W. Smith, Mater. Sci. Technol 8 (1992) 537.
[49] K. Takeda, N. Nakada, T. Tsuchiyama, S. Takaki, ISIJ Int. 48 (2008) 1122.
[50] J. Takahashi, K. Kawakami, K. Ushioda, S. Takaki, N. Nakata, T. Tsuchiyama, Scripta Mater. 66 (2012) 207.
[51] D. Raabe, F. Heringhaus, U. Hangen, G. Gottstein, Z. Metallk. 86 (1995) 405.
[52] D. Raabe, F. Heringhaus, U. Hangen, G. Gottstein, Acta Metall. Mater. 43 (1995) 407.
[53] A. Goyal, E.D. Specht, D.M. Kroeger, Appl. Phys. Lett. 68 (1996) 711.
[54] R.Z. Valiev, R.K. Islamgaliev, I.V. Alexandrov, Prog. Mater. Sci. 45 (2000) 103.
[55] J.C.M. Li, J. Appl. Phys. 33 (1962) 2958.
[56] P.A. Beck, J. Appl. Phys. 20 (1949) 633.
[57] R.W. Cahn, Proc. Phys. Soc. London Sect. A 63 (1950) 323.
[58] A.H. Cottrell, in: B. Chalmers (Ed.), Theory of Dislocations, Progress in Metal Physics, 4, Pergamon Press, London, 1953, pp. 251–255.

[59] W. Blum, C. Schlögl, M. Meier, Z. Metallk. 86 (1995) 631.
[60] J. Fridberg, L.E. Trndahl, M. Hillert, Jernk. Ann. 153 (1969) 263.
[61] L. Uray, M. Menyhárd, Phys. Status Solidi (a) 84 (1984) 65.
[62] R. Kirchheim, Acta Mater. 55 (2007) 5129.
[63] R. Kirchheim, Acta Mater. 55 (2007) 5139.
[64] A.V. Galina, V.Y. Fradkov, L.S. Schvindlerman, Fiz. Metallov Metalloved 63 (1987) 1220.
[65] M. Upmanyu, D.J. Srolovitz, L. Shvindlerman, G. Gottstein, Acta Mater. 55 (2002) 1405.
[66] G. Gottstein, L.S. Shvindlerman, B. Zhao, Scripta Mater. 62 (2010) 914.
[67] A. Hasnaoui, H.V. Swygenhoven, P.M. Derlet, Acta Mater. 50 (2002) 3927.
[68] R.Z. Valiev, A.V. Sergueeva, A.K. Mukherjee, Scripta Mater. 49 (2003) 669.
[69] Y.M. Wang, S. Cheng, Q.M. Wei, E. Ma, T.G. Nieh, A. Hamza, Scripta Mater. 51 (2004) 1023.
[70] X. Huang, N. Hansen, N. Tsuji, Science 312 (2006) 249.
[71] E. Smith, Int. J. Fract. Mech. 4 (1968) 132.